Flow stability in shallow droplets subject to localized heating of the bottom plate

Khang Ee Pang,[1] Charles Cuvillier,[2] Yutaku Kita,[3,4] and Lennon Ó Náraigh[1,*]
[1]*School of Mathematics and Statistics, University College Dublin, Ireland*
[2]*UMA Applied Mathematics Department, ENSTA Paris, France*
[3]*Department of Engineering, King's College London, United Kingdom*
[4]*International Institute for Carbon-Neutral Energy Research (WPI-I^2 CNER), Kyushu University, 744 Motooka, Nishi-ku, Fukuoka 819-0395, Japan*

(Received 18 July 2023; accepted 11 December 2023; published 16 January 2024)

We investigate theoretically the stability of thermo-capillary convection within a droplet when subject to localized heating from below. To model the droplet, we use a mathematical model based on lubrication theory. We formulate a base-state droplet profile, and we examine its stability with respect to small-amplitude perturbations in the azimuthal direction. Such linear stability analysis reveals that the base state is stable across a wide parameter space. We carry out transient simulations in three spatial dimensions: the simulations reveal that when the heating is slightly off-centered with respect to the droplet center, vortices develop within the droplet. The vortices persist when the contact line is pinned. These findings are consistent with experimental studies of locally heated sessile droplets.

DOI: 10.1103/PhysRevFluids.9.014003

I. INTRODUCTION

When the surface tension of a droplet or a film varies inhomogeneously, surface-tension gradients occur, which induce a flow inside the fluid. Such surface-tension gradients can arise due to differential evaporation of different components in a binary fluid [1], or the presence of surfactants [2]. Similarly, the presence of a temperature gradient along the surface of the droplet or film [3] may drive such a flow, in which case the result is referred to as a thermocapillary flow. Often, a convective flow is the result of such surface-tension gradients, in which the fluid flows in tesselated convection cells, in a phenomenon referred to as Bénard–Marangoni convection [4]. Tesselated Bénard–Marangoni cells arise when the temperature gradient is normal to the interface. The role of surface tension and surface-tension gradient in the production of such flows (as opposed simply to buoyancy-driven convection) was first identified by Marangoni in his Ph.D. thesis in 1865 [5]. Since then, the study of such eponymous *Marangoni flows*—driven by gradients in surface tension—has been a source of much scientific interest, motivated by the fundamental physics of capillarity and wetting, as well as the practical industrial applications. The focus of the present work is on Marangoni flows driven by temperature gradients, the understanding of which is important for welding, crystal growth, and electron-beam melting [6].

In this work, we are concerned with the theoretical modeling of the flow inside a sessile droplet subject to localized heating from below. Such local heating causes a difference in the surface tension on the droplet surface, which drives a Marangoni current. The creation of such flows inside droplets can greatly enhance the heat transfer across the droplet. Hence, understanding these flows is important for optimizing various industrial processes where droplets play a role, for instance, spray

*onaraigh@maths.ucd.ie

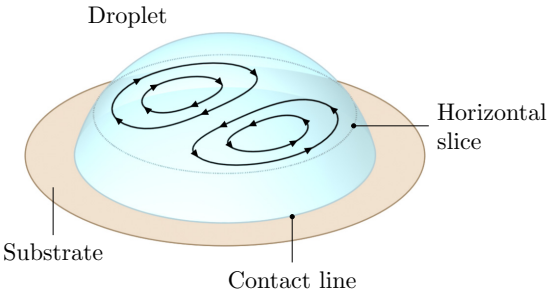

FIG. 1. Schematic description of the experimentally observed flow in a locally heated sessile droplet.

cooling [7], and the operation of electronic and rheological devices in microgravity conditions where buoyancy effects are negligible [8].

Thermocapillary flows induced by localized heating been observed experimentally in millimeter-sized water droplets [9,10]. In particular, these experiments reveal that when such droplets are heated from below by a localized heat source targeted at the droplet center, a vortex pair perpendicular to the substrate is observed. The aim of this work is to obtain some theoretical understanding to explain the onset of such vortices. A schematic description of the vortex pair is shown in Fig. 1.

The experimental results in Refs. [9,10] concern hydrophobic substrates, where the equilibrium contact angle is around 110°. This particular setup is difficult to model analytically. Therefore, as a first attempt to understand theoretically the origin of the vortex pair, we investigate hydrophilic substrates, where the equilibrium contact angle is small, and where lubrication theory can be used for the analytical modeling. As such, the aim of the present work is to gain qualitative insights into the formation of the vortex pair in the locally heated droplet rather than precise quantitative insights. In particular, we seek to determine if, given an axisymmetric equilibrium solution for the locally heated droplet in lubrication theory, can linear stability analysis explain the onset of thermo-capillary flows in the azimuthal direction? In other words, is the axisymmetric equilibrium solution susceptible to symmetry-breaking via linear instability? The answer to this question—at least in lubrication theory—turns out to be in the negative. Hence, in this work, we also investigate other mechanisms which can produce the kind of nonaxisymmetric flow shown in Fig. 1.

We focus in this work solely on thermo-capillary effects: as such, we do not consider evaporation, although this could be considered in future work. The motivation for doing so is based on the experimental results, where the onset of vortices in the azimuthal direction is an extremely fast process, taking place on the timescale of seconds, whereas the timescale for significant evaporation to occur is of the order of minutes.

Lubrication theory is a key tool in analyzing thermo-capillary flows in thin films and droplets—provided the latter possesses a sufficiently small equilibrium contact angle. Lubrication theory refers to a particular limiting geometry where the length scale of flow variations in the film (or droplet) in the lateral direction greatly exceeds that in the vertical direction. In such a scenario, there is a natural small parameter, being the ratio of these two length scales, which enables an expansion of the Navier–Stokes equations [11]. At lowest order in the expansion, one obtains a single equation for the height of the film (or droplet) as a function of the lateral variations and time. The flow inside the film (or droplet) is Stokes flow, for which analytical expressions can be obtained.

Following this approach, Ehrhard and Davis [3] have studied the spreading of three-dimensional (3D) axisymmetric droplets on a homogeneously heated substrate. The heating from below induces a classical, axisymmetric Marangoni current such as the one shown schematically in Fig. 2. Erhard and Davis further found that the Marangoni current impedes the spreading of the droplets. For fixed droplet volume and contact angle, increasing the Marangoni number results in a lower equilibrium droplet radius. The theoretical predictions agreed well with experiments. Similarly, Tan *et al.* [12] and Van Hook *et al.* [13] studied the rupturing of two-dimensional (2D) and 3D

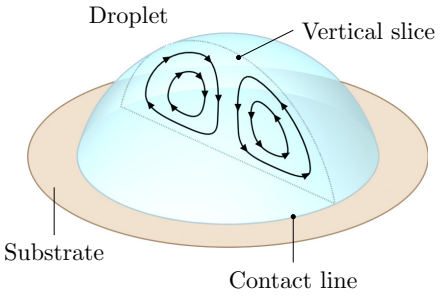

FIG. 2. The classical axisymmetric Marangoni current observed in prior works, in the case of uniform heating of the substrate.

thin films, respectively, on a substrate subjected to a spatially periodic heat source. An attractive van der Waals potential $\phi = Ah^{-3}$ is used to model the dewetting. Local dewetting of the film is observed in high-temperature regions. A critical Marangoni number is found above which the deformed steady-state becomes unstable and rupturing occurs. Gravity is found to be stabilizing and delays the onset of rupture. Film rupture driven by Marangoni flows in the case of uniformly heated substrates has also been investigated [14]. Bostwick [15] extended the work in Ref. [3] to account for temperature variations in the substrate in the radial direction; both linear and logarithmic temperature profiles were looked at, allowing for both cooling and heating as one moves away from the droplet center. Multiple stable equilibrium droplet solutions exist in the case of cooling of the droplet core; on the other hand, when the droplet is heated at the core, no such bistability is found. The present work extends this analysis by considering highly localized heating at the droplet core.

Beside lubrication theory, direct numerical simulations (DNSs) have been used to study the dynamics of droplet on heated substrate. Sáenz *et al.* [16] simulated 3D asymmetric droplets on a homogeneously heated substrate. The asymmetry of the droplet shape is imposed by contact-line pinning. For highly asymmetric droplets, a vortex pair perpendicular to the substrate was observed. Shi *et al.* [17] investigated a thin droplet on a homogeneously heated substrate with a spherical-cap interface. They observed the development of multiple hexagonal Bénard–Marangoni convection cells above a critical Marangoni number. Lu *et al.* [18] studied evaporating droplets in an axisymmetric setting. The free surface is modeled as a spherical cap with constant radius and decreasing volume depending on the evaporation flux. For millimeter-sized droplets, they found that the Marangoni convection is dominant over the natural convection by about three orders of magnitude. Lee *et al.* [19] used a similar method to study the effect of localized heating. When the droplet is heated at the center, they observed a reversal of the convection flow compared with the homogeneously heated droplet where the fluid falls at the center of the droplet.

The work is organized as follows: In Sec. II we present the theoretical model along with the key assumptions. In Sec. III we look at axisymmetric solutions of the model—including droplet and ring solutions. We study the linear stability of the droplet solution with respect to small-amplitude perturbations in the azimuthal direction. In Sec. IV we use transient numerical simulations to understand in more detail the linear stability of the droplet solution. We also investigate the emergence of the ring solution in certain regions of parameter space. Having concluded from these investigations the droplet solution is stable to small-amplitude disturbances, in Sec. V we look at a second possible mechanism for the generation of Marangoni currents in the azimuthal direction—namely, a small perturbation of the localized heat source away from the droplet center. We show such currents persist only in the case of pinned droplets. The implications of our findings for the experimental knowledge already in the literature are discussed and concluding remarks given in Sec. VI.

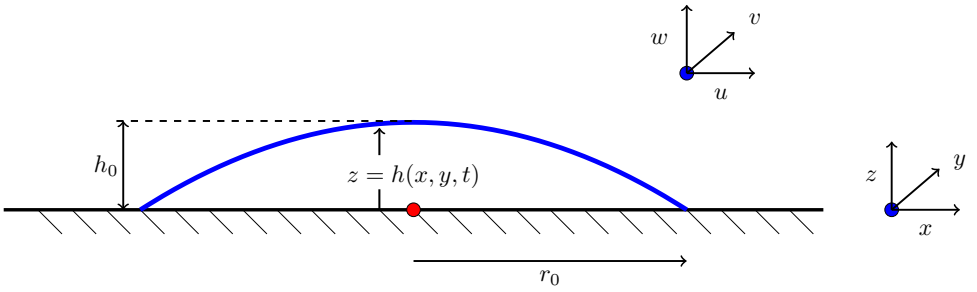

FIG. 3. Schematic description of the fluid mechanical problem of droplet spreading, as derived from the Navier–Stokes equations in the lubrication limit.

II. THEORETICAL FORMULATION

In this section we introduce the mathematical model to describe locally heated droplets. We use standard lubrication theory in three spatial dimensions. We emphasize that such an approach is only valid for droplets with a small equilibrium contact angle (that is, droplets on a hydrophilic surface). Another approach may be required for droplets on a hydrophobic surface. The setup is shown schematically in Fig. 3. We first of all derive an equation for the height $h(x, y, t)$ of the droplet and then derive an equation for the temperature inside the droplet.

A. Expression for droplet height

To derive an expression for the droplet height $h(x, y, t)$, we use standard lubrication theory in three spatial dimensions. This involves the use of a small parameter ϵ, being the ratio of the vertical length scale to the horizontal length scale. The meaning of ϵ in the context of droplets is shown schematically in Fig. 3, where ϵ is defined as h_0/r_0. In this context, the droplet sits on a substrate at $z = 0$ and experiences localized heating. No-slip boundary conditions apply at the substrate; interfacial conditions at the interface between the liquid and the surrounding atmosphere will be developed herein.

The starting point for the derivation is then the incompressibility condition:

$$\frac{\partial u}{\partial x} + \frac{\partial v}{\partial y} + \frac{\partial w}{\partial z} = 0. \tag{1}$$

Following standard integration steps [11], Eq. (1) can be recast as

$$\frac{\partial h}{\partial t} + \frac{\partial}{\partial x}(\langle u\rangle h) + \frac{\partial}{\partial y}(\langle v\rangle h) = 0, \tag{2}$$

where $\langle u\rangle$ and $\langle v\rangle$ are the depth-averaged velocities,

$$\langle u\rangle = \frac{1}{h}\int_0^h u\mathrm{d}z, \quad \langle v\rangle = \frac{1}{h}\int_0^h v\mathrm{d}z. \tag{3}$$

To constitute the depth-averaged velocities, we assume Stokes flow in the droplet; this assumption is valid provided ϵ is sufficiently small. In this case, the following momentum balance conditions are obtained:

$$-\frac{\partial p}{\partial x} + \mu\frac{\partial^2 u}{\partial z^2} - \frac{\partial \Phi}{\partial x} = 0, \tag{4a}$$

$$-\frac{\partial p}{\partial y} + \mu\frac{\partial^2 v}{\partial z^2} - \frac{\partial \Phi}{\partial y} = 0, \tag{4b}$$

$$-\frac{\partial p}{\partial z} - \frac{\partial \Phi}{\partial z} = 0. \tag{4c}$$

Here, p is the fluid pressure and Φ is the potential function associated with the van der Waals forces between the droplet and the substrate; these forces in turn fix the precursor-film thickness and the equilibrium contact angle.

Following a standard sequence of steps [11], Eq. (4) can be integrated once to produce:

$$\mu \frac{\partial^2}{\partial z^2}(u, v) = \nabla(p + \Phi) = \nabla(-\gamma_0 \nabla^2 h + \Phi|_h). \tag{5}$$

Here, $\nabla = (\partial_x, \partial_y)$ and $\nabla^2 = \partial_x^2 + \partial_y^2$ are the gradient and Laplacian operator in the xy-plane, and γ_0 is a constant reference value of the surface tension. The right-hand side of Eq. (5) is independent of z. As such, Eq. (5) can be integrated twice to yield expressions for u and v. We use the no-slip boundary condition at $z = 0$, and we further use the interfacial condition:

$$\mu \frac{\partial}{\partial z}(u, v) = \nabla\gamma \quad \text{at } z = h, \tag{6}$$

where $\nabla\gamma$ is the surface-tension gradient (independent of z). Hence, Eq. (5) integrates to

$$\mu(u, v) = z\nabla\gamma + \left(\tfrac{1}{2}z^2 - hz\right)\nabla(-\gamma_0 \nabla^2 h + \Phi|_h). \tag{7}$$

The expressions for u and v in Eq. (7) depend on x and y. These can be depth-averaged to give

$$\mu\langle u\rangle = \frac{1}{2}h\frac{\partial\gamma}{\partial x} - \frac{1}{3}h^2\frac{\partial}{\partial x}(-\gamma_0\nabla^2 h + \Phi|_h),$$
$$\mu\langle v\rangle = \frac{1}{2}h\frac{\partial\gamma}{\partial y} - \frac{1}{3}h^2\frac{\partial}{\partial y}(-\gamma_0\nabla^2 h + \Phi|_h).$$

The depth-averaged velocities can now be substituted back into Eq. (2) to give

$$\mu\frac{\partial h}{\partial t} + \nabla\cdot\left\{\frac{1}{2}h^2\nabla\gamma - \frac{1}{3}h^3\nabla(-\gamma_0\nabla^2 h + \Phi|_h)\right\} = 0. \tag{8}$$

B. Expression for the temperature profile

Quite generally, the droplet temperature T satisfies an advection-diffusion equation. However, given the small parameter $\epsilon = h_0/r_0$, the standard scaling arguments [11] in lubrication theory apply, and the advection-diffusion equation reduces to

$$\frac{\partial^2 T}{\partial z^2} = 0, \tag{9}$$

with solution

$$T = A(x, y, t)z + B(x, y, t). \tag{10}$$

Here, A and B are determined from boundary conditions.

We first of all address the boundary condition at the substrate at $z = 0$. We assume that the substrate is heated in an inhomogeneous fashion, such that the substrate temperature T_s is given by

$$T_s(x, y) = \langle T_s\rangle + (\Delta T_s)\tilde{T}_s(x, y), \tag{11}$$

where $\langle T_s\rangle$ denotes the mean temperature and $\Delta T_s = \max T_s - \min T_s$ is the maximum temperature difference across the substrate. We similarly rewrite the temperature inside the droplet as

$$T(x, y, z) = \langle T_s\rangle + \Delta T_s[\tilde{T}_s(x, y) + \tilde{T}(x, y, z)]. \tag{12}$$

Continuity of temperature at the interface between the liquid film and the substrate means that $T = T_s$ at $z = 0$, hence $\tilde{T} = 0$ at $z = 0$. We furthermore assume that the film temperature satisfies a

Robin boundary condition at $z = h(x, y, t)$; this corresponds to the application of Newton's law of cooling at the interface:

$$-k_{th}\frac{\partial T}{\partial z} = \alpha_{th}(T - T_g), \quad z = h(x, y, t). \tag{13}$$

Here, k_{th} is the thermal conductivity of the film, α_{th} is the heat-transfer coefficient, and T_g is the temperature of the gas surrounding the film. Substituting Eq. (12) into Eq. (13) gives

$$-k_{th}\frac{\partial \tilde{T}}{\partial z} = \alpha_{th}\left[\tilde{T} + \tilde{T}_s(x, y) + \frac{\langle T_s\rangle - T_g}{\Delta T_s}\right], \tag{14}$$

at $z = h$. Rearranging, this reads

$$-\frac{\partial \tilde{T}}{\partial z} = \frac{\mathrm{Bi}}{h_0}[\tilde{T} + \tilde{T}_s(x, y) + \Theta], \quad z = h, \tag{15}$$

where $\Theta = (\langle T_s\rangle - T_g)/\Delta T_s$ is the scaled temperature difference between the substrate and the surrounding gas, h_0 is the vertical length scale of the system, and $\mathrm{Bi} = \alpha_{th}h_0/k_{th}$ is the Biot number.

By linearity, $\tilde{T}$ satisfies the diffusion equation (9) also. Hence, $\tilde{T}$ also has the form $\tilde{A}z + \tilde{B}$. Applying the boundary condition $\tilde{T} = 0$ at $z = 0$, the temperature profile $\tilde{T}$ becomes

$$\tilde{T} = \tilde{A}(x, y, t)z. \tag{16}$$

Applying the boundary condition (15), we obtain

$$\tilde{A} = -\frac{\mathrm{Bi}[\tilde{T}_s(x, y) + \Theta]}{1 + \mathrm{Bi}\tilde{h}}\frac{1}{h_0}, \tag{17}$$

hence

$$\tilde{T}(x, y, z, t; h) = -\frac{\mathrm{Bi}[\tilde{T}_s(x, y) + \Theta]}{1 + \mathrm{Bi}\tilde{h}}\tilde{z}, \tag{18}$$

where $\tilde{z} = z/h_0$ and $\tilde{h} = h/h_0$ are in their dimensionless form. We also explicitly denote the dependence on the interface height h. The complete temperature profile in the film therefore reads:

$$T(x, y, z, t; h) = \langle T_s\rangle + \Delta T_s\left[\tilde{T}_s(x, y) - \frac{\mathrm{Bi}(\tilde{T}_s(x, y) + \Theta)}{1 + \mathrm{Bi}\tilde{h}}\tilde{z}\right]. \tag{19}$$

The temperature on the surface of the film is therefore

$$T|_{z=h} = \langle T_s\rangle + (\Delta T_s)\vartheta(x, y, t; h), \tag{20}$$

where ϑ is the nondimensional temperature variation at the interface given by

$$\vartheta(x, y, t; h) = \frac{\tilde{T}_s(x, y) - \Theta\mathrm{Bi}\tilde{h}}{1 + \mathrm{Bi}\tilde{h}}. \tag{21}$$

C. Final model and nondimensionalization

Equation (8) for the droplet height involves the temperature implicitly, via the surface-tension gradient $\nabla\gamma$. We now make this dependence explicit, thereby reducing the model down to a single equation. To do this, we assume an explicit linear dependence for the surface tension on temperature:

$$\gamma = \gamma_0 - \frac{\gamma_1}{\Delta T_s}(T - T_{\mathrm{ref}}), \quad z = h(x, y, t), \tag{22}$$

where γ_0 is the reference level of surface tension, $\gamma_1 > 0$ is a positive constant, and T_{ref} is a reference temperature. Although γ_0 depends on T_{ref}, T_{ref} does not appear directly in the final model; only γ_0

and $\nabla\gamma$ are important. Hence,

$$\nabla\gamma = -\frac{\gamma_1}{\Delta T_s}\nabla T, \quad z = h(x, y, t). \tag{23}$$

Using Eq. (20), this becomes

$$\nabla\gamma = -\gamma_1 \nabla\vartheta(x, y, t; h). \tag{24}$$

Substitution into Eq. (8) yields

$$\mu\frac{\partial h}{\partial t} + \nabla\cdot\left[-\frac{1}{2}\gamma_1 h^2\nabla\vartheta - \frac{1}{3}h^3\nabla(-\gamma_0\nabla^2 h + \Phi|_h)\right] = 0. \tag{25}$$

We nondimensionalize Eq. (25), using r_0 and h_0 as length scales. For the meaning of these length scales, see Fig. 3; the ratio $\epsilon = h_0/r_0$ is much less than one, corresponding to the limiting case where lubrication theory is valid. We introduce corresponding nondimensional variables:

$$\tilde{x} = \frac{x}{r_0}, \quad \tilde{y} = \frac{y}{r_0}, \quad \tilde{z} = \frac{z}{h_0}, \quad \tilde{h} = \frac{h}{h_0}, \quad \tilde{\nabla} = r_0\nabla.$$

Hence, Eq. (25) becomes

$$\mu h_0\frac{\partial\tilde{h}}{\partial t} + \tilde{\nabla}\cdot\left[-\frac{1}{2}\gamma_1\epsilon^2\tilde{h}^2\tilde{\nabla}\vartheta - \frac{1}{3}\epsilon^2 h_0\tilde{h}^3\tilde{\nabla}\left(-\frac{\gamma_0 h_0}{r_0^2}\tilde{\nabla}^2\tilde{h} + \Phi|_h\right)\right] = 0. \tag{26}$$

We divide by $\gamma_0\epsilon^4$ to obtain

$$\frac{\mu h_0}{\gamma_0\epsilon^4}\frac{\partial\tilde{h}}{\partial t} + \tilde{\nabla}\cdot\left[-\frac{1}{2}\frac{\gamma_1}{\gamma_0\epsilon^2}\tilde{h}^2\tilde{\nabla}\vartheta - \frac{1}{3}\tilde{h}^3\tilde{\nabla}\left(-\tilde{\nabla}^2\tilde{h} + \frac{h_0}{\gamma_0\epsilon^2}\Phi|_h\right)\right] = 0. \tag{27}$$

Thus we are motivated to scale the time and the potential by

$$\tilde{t} = \frac{\gamma_0\epsilon^4}{\mu h_0}t, \quad \tilde{\phi} = \frac{h_0}{\gamma_0\epsilon^2}\Phi|_h, \tag{28}$$

and the dimensionless Marangoni number is identified as

$$\mathrm{Ma} = \frac{\gamma_1}{\gamma_0\epsilon^2}. \tag{29}$$

Finally, with the tildes dropped, the dimensionless thin-film equation reads

$$\frac{\partial h}{\partial t} + \nabla\cdot\left[-\frac{1}{2}\mathrm{Ma}h^2\nabla\vartheta - \frac{1}{3}h^3\nabla(-\nabla^2 h + \phi)\right] = 0, \tag{30a}$$

and

$$\vartheta(x, y, t; h) = \frac{T_s(x, y) - \Theta\mathrm{Bi}h}{1 + \mathrm{Bi}h}. \tag{30b}$$

Equation (30) is the final model which forms the basis of the analysis in the rest of the paper.

D. Discussion

In formulating Eq. (30), we have neglected droplet evaporation. The motivation for doing so is based on the experimental results in Refs. [9,10]. In these works, the onset of vortices in the azimuthal direction is an extremely fast process, taking place on the timescale of seconds, whereas the timescale for significant evaporation to occur is of the order of minutes. Furthermore, the model in Eq. (30) does not account for gravity. This is again motivated by the experimental results, where the convection is Marangoni-driven, not buoyancy-driven (as confirmed Refs. [9], wherein the convection patterns are the same whether the droplet is upright or pendant).

E. Methodology

We solve various forms of Eq. (30) numerically to investigate mechanisms by which the axisymmetry of the time-independent base state may be lost. This calls for a number of numerical techniques, including a shooting method for the computation of the base state, eigenvalue analysis for a linear stability analysis of the base state, and transient three-dimensional numerical simulations. As these methodologies are distinct and context-dependent, these are best described as they are required, throughout the paper. Further technical details on the numerical methods are presented in the Appendixes.

III. AXISYMMETRIC BASE STATE AND LINEAR STABILITY ANALYSIS

In this section we solve Eq. (30) in an axisymmetric configuration corresponding to a droplet experiencing localized heating at the substrate. We are interested both in a steady-state solution, and a configuration comprising a small perturbation away from the steady state. This second configuration involves the development of a linear stability analysis around the axisymmetric steady state. In this context, it is possible to set $\phi = 0$, corresponding to a pinned droplet with a prescribed equilibrium contact angle.

A. Base state

We first look at equilibrium solution ($\partial_t h = 0$) in an axisymmetric configuration about the z axis by considering surface temperature $T_s = T_s(r)$, depending only on $r = (x^2 + y^2)^{1/2}$. In this case, Eq. (30) reduces to a one-dimensional nonlinear ordinary differential equation (ODE) given by

$$\frac{1}{r}\frac{\partial}{\partial r}\left\{-\frac{1}{2}\mathrm{Ma}h^2 r\vartheta' + \frac{1}{3}h^3 r\frac{\partial}{\partial r}\left[\frac{1}{r}\frac{\partial}{\partial r}\left(r\frac{\partial h}{\partial r}\right)\right]\right\} = 0, \tag{31a}$$

defined on the domain $r \in [0, r_*]$ where $r = r_*$ is the contact-line position. Here, $\vartheta' = (\partial\vartheta/\partial h)(\partial h/\partial r) + (\partial\vartheta/\partial r)$. The boundary conditions are given by

$$\partial_r h = 0 \quad \text{at } r = 0, \tag{31b}$$

$$h = 0, \quad \partial_r h = -\alpha \quad \text{at } r = r_*. \tag{31c}$$

Here, α is the scaled equilibrium contact angle. The scaling is done using a standard approach of lubrication theory, which is described briefly in Appendix A. The prescription of a fixed equilibrium contact angle in this case is equivalent to a precursor-film model with a van der Waals potential. Equation (31c) refers to the boundary condition at the droplet edge $r = r_*$. In view of the lubrication-theory scaling, we take $r_* = 1$. By integrating Eq. (31) with respect to r once and asserting $h(1) = 0$, we obtain a third-order nonlinear ODE

$$h''' = \frac{3}{2}\mathrm{Ma}\frac{\vartheta'}{h} - \frac{h''}{r} + \frac{h'}{r^2}, \quad 0 < r < 1. \tag{32}$$

Here, the primes denote derivatives with respect to r. Equation (32) is solved numerically using a shooting method and/or `BVP4C` in MATLAB. For $\mathrm{Ma} \neq 0$, the third derivative h''' becomes singular at the boundary $r = 1$. However, the third derivative remains finite in the interior of the domain, where the ODE is defined. A regularization technique (with regularization parameter δ) described in Appendix B ensures an accurate numerical solution which accounts for this singular behavior. In cases where a classical (or strong) solution of the ODE exists, the regularized solution converges to a well-defined limit as $\delta \to 0$. In contrast, the apparent singularity in the ODE as $r \to 0$ is cosmetic, because of the particular choice of boundary conditions in Eq. (31b).

Once the solution $h(r)$ is obtained, the Stokes stream function can be computed:

$$\psi(r, z; h) = -r\int_0^z u_r(r, \tilde{z}; h)\mathrm{d}\tilde{z} = r\left[\frac{1}{2}\mathrm{Ma}z^2\vartheta' - \left(\frac{1}{2}hz^2 - \frac{1}{6}z^3\right)\frac{\partial}{\partial r}\left(h'' + \frac{h'}{r}\right)\right], \tag{33}$$

valid for $0 \leqslant r \leqslant 1$ and $0 \leqslant z \leqslant h(r)$.

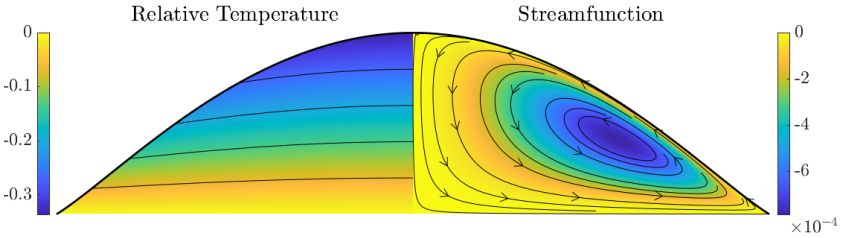

(a) Homogeneous heating $T_s(r) = 0$

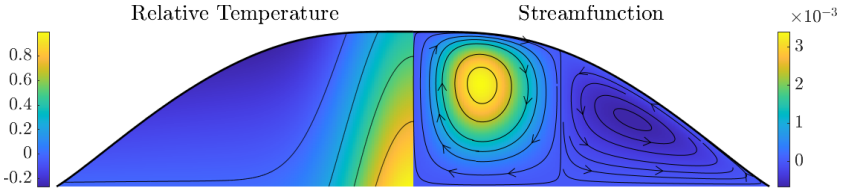

(b) Localized heating $T_s(r) = \mathrm{e}^{-r^2/0.2^2}$

FIG. 4. Equilibrium solutions for different heat sources. We take $\alpha = 0.6$. All other parameters (Ma, Bi, Θ) are taken to be unity.

A first set of results is shown in Fig. 4. For these results, we have taken $\alpha = 0.6$; all other parameters (Ma, Bi, Θ) are taken to be unity. The top panel shows homogeneous substrate heating, with $T_s(r) = 0$. The bottom panel shows inhomogeneous substrate heating, with $T_s(r) = \mathrm{e}^{-r^2/0.2^2}$. The left-hand side of each panel shows the temperature within the droplet $T(r, z)$ given by Eq. (19) (with $\Delta T_s = 1$ and the $\langle T_s \rangle$ term dropped). The right-hand side of each panel shows the Stokes stream function $\psi(r, z; h)$. In case of homogeneous heating, a temperature gradient emerges such that the base of the droplet is relatively hot compared with the top of the droplet. The stream function shows one convective cell with flow in the anticlockwise direction—consistent with the classical description in Fig. 2. In contrast, in case of localized heating (bottom panel), the temperature decreases both with vertical distance and radial distance from the droplet center. Furthermore, the stream function indicates two convective cells in the droplet. The outer convective cell has a flow with the same anticlockwise orientation as in the homogeneously heated case. However, this flow is weaker compared with the flow in the inner cell. The flow in the inner cell is clockwise, such that the flow near to the droplet's axis of symmetry is upward. This consistent with direct numerical simulation on locally heated droplets [19]. A further (albeit more minor) distinction between the two panels is that the maximum height of the homogeneously heated droplet is higher than that of the locally heated droplet.

Figure 5 shows the equilibrium droplet volume for various values of Marangoni number Ma and equilibrium contact angle α. As per Eq. (31), the radius r_* is fixed and set to $r_* = 1$ in the chosen scaling. Hence, the droplet is pinned and the triple point is fixed at a set radius; the volume required to realize such a droplet with a given contact angle is thus an outcome of the computations. Furthermore, in this figure, the contact angle is an intrinsic property of the fluid (more precisely, of the fluid-air-substrate trio). Similarly, the Marangoni number depends on the ratio γ_1/γ_0 and, hence, on the intrinsic fluid properties [although the small parameter ϵ enters into the definition of Ma also, cf. Eq. (29)]. Hence, each point in the flow-pattern map can be thought of as corresponding to a different working fluid. From the figure, it can be seen that the droplet volume and height are positively correlated to α and Ma. There is also lower bound for the possible equilibrium droplet size at fixed Ma. Crucially, for small droplet volume and fixed Ma, there is a critical α value where the localized heating causes the droplet to rupture and the classical (or strong) solution of the

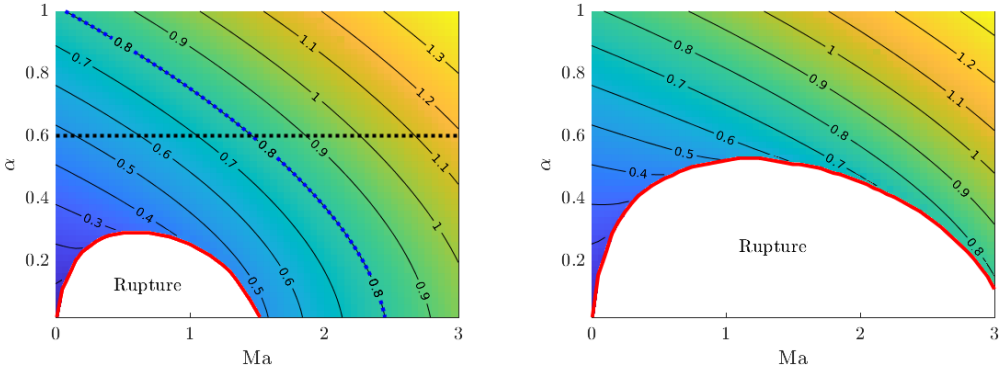

(a) $T_s(r) = \mathrm{e}^{-r^2/0.2^2}$ (b) $T_s(r) = \mathrm{e}^{-r^2/0.3^2}$

FIG. 5. Contour plot of the equilibrium droplet volume as a function of equilibrium contact angle α and Marangoni number Ma, for (a) $s = 0.2$, and (b) $s = 0.3$. Other physical parameters are $(\mathrm{Bi}, \Theta) = (1, 1)$. Empty regions correspond to cases where the droplet ruptures. The broken-line curves in panel (a) indicate different paths through the parameter space used in the linear stability analysis: a constant-α path, and a constant-volume path.

boundary-value problem valid on $0 < r < 1$ ceases to exist. In this case, a piecewise solution

$$h(r) = \begin{cases} 0, & r < r_1 \\ f(r), & r \geqslant r_1 \end{cases} \tag{34}$$

can be found, where $f(r)$ satisfies the ordinary differential equation (32) with boundary conditions $f(r_1) = f(1) = 0$, $f'(r_1) = \alpha$, $f'(1) = -\alpha$. Thus, Eq. (34) is a weak solution of Eq. (31), with a jump discontinuity in h' at $r = r_1$. Alternatively, $f(r)$ may be viewed as a classical solution of the ODE on the restricted domain $(r_1, 1)$. Figure 6 shows the loss of the classical solution and the profile $h(r)$ in one particular parameter case. The piecewise solution has the appearance of a ring,

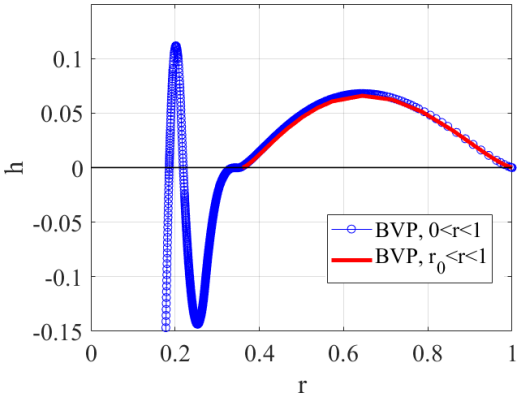

FIG. 6. Plot showing the occurrence of a weak solution at a critical value of α, for fixed Ma. Parameter values: $\mathrm{Ma} = 1$, $\alpha = 0.1$, and $s = 0.2$. The blue curve refers to the classical solution of the regularized boundary-value problem on $0 < r < 1$ (regularization parameter: $\delta = 10^{-4}$). The regularized classical solution fails: h turns negative, and the numerical solution does not converge as the regularization parameter tends to zero (in nonsingular cases, the regularization technique does converge, and h remains non-negative). The red curve has been generated using `BVP4C` in MATLAB and refers to the piecewise solution [Eq. (34)], which is non-negative on $r_1 < r < 1$, and which is zero in the core region $0 \leqslant r \leqslant r_1$.

with $h(0) = 0$, hence the designation of the blank regions in Figure 5 as "ring rupture." We develop precise criteria for the avoidance of ring rupture (and also, for its onset) below, in a mathematical analysis of the base state. The evolution of the film towards ring rupture is explored in further detail in Sec. IV, in the context of transient numerical simulation.

B. Mathematical analysis of the base state

Equation (32) is a nonlinear third-order ODE, the analytical solution of which is not at all apparent. However, it is possible to understand the behavior of the solutions in a qualitative sense by multiple applications of integration by parts. This approach is particularly fruitful in the case where $\mathrm{Bi} = 0$, which we present below. Where appropriate, we comment on the applicability of the results to the case where $\mathrm{Bi} > 0$.

A starting point is to integrate Eq. (32) between a general value of r and the boundary at $r = 1$. We use integration by parts and we apply the pertinent boundary conditions. This gives

$$\tfrac{1}{2}[3\mathrm{Ma}\Delta T_s(r) - \alpha^2] = h(r)\nabla^2 h(r) + J_r^2 - \tfrac{1}{2}[h'(r)]^2, \quad \Delta T_s(r) = T_s(r) - T_s(1). \tag{35}$$

Here, we have used the fact that $\vartheta = T_s$ in the case where $\mathrm{Bi} = 0$. Furthermore, we have introduced the notation

$$J_r^2 = \int_r^1 \frac{1}{r}[h'(r)]^2 \mathrm{d}r. \tag{36}$$

We evaluate Equation (35) at $r = 0$, and use the fact that $h'(0) = 0$. This gives

$$\tfrac{1}{2}[3\mathrm{Ma}\Delta T_s(0) - \alpha^2] = 2h(0)h''(0) + J_0^2 \tag{37}$$

[the factor of two comes from an application of L'Hôpital's rule to $\nabla^2 h(r)$ evaluated at $r = 0$]. Here, J_0^2 refers to J_r^2 evaluated at $r = 0$. Hence, if

$$3\mathrm{Ma}\Delta T_s(0) - \alpha^2 < 0. \tag{38}$$

then $h(0)h''(0) < 0$. This yields two results:

(1) a *no-rupture condition* $h(0) \neq 0$;

(2) the condition $h''(0) < 0$, such that $r = 0$ is a local maximum.

Hence, Eq. (38) is a necessary condition for $r = 0$ to be a local maximum.

The analogous result in the case where $\mathrm{Bi} > 0$ is $(1/2)[3\mathrm{Ma}\Delta\vartheta(0) - \alpha^2] = h(0)h''(0) + J_0^2$, where $\Delta\vartheta(0) = \vartheta(0) - \vartheta(1)$. Since ϑ is monotone decreasing in h, we have that $\Delta\vartheta(0) \leqslant \Delta T_s(0)$. Hence, Eq. (38) remains a necessary condition for $h(0)$ to be a maximum, in the case $\mathrm{Bi} > 0$.

For fixed Ma, and below a critical value of α, $h(0)$ ceases to be a local maximum and a "hump" solution emerges (e.g., Fig. 7). To analyze such solutions, we revert to $\mathrm{Bi} = 0$ and we look at the case $3\mathrm{Ma}\Delta T_s(0) - \alpha^2 < 0$. To make further progress, we must estimate J_0^2 in Eq. (37) and for this purpose we approximate $h(r)$ as $\eta + ar^2 + br^4$. We apply $h(1) = 0$ and $h'(1) = -\alpha$. This fixes a and b. We substitute the resulting expressions into the formula for J_0^2 and obtain the approximation $J_0^2 \approx -(4/3)\eta^2 + (1/3)\eta\alpha + (1/6)\alpha^2$. We substitute this expression back into Eq. (37) and obtain

$$\tfrac{1}{2}[3\mathrm{Ma}\Delta T_s(0) - \alpha^2] = -\tfrac{16}{3}\eta^2 + \tfrac{4}{3}\eta\alpha + \tfrac{1}{6}\alpha^2. \tag{39}$$

This is a quadratic equation for η. By checking the discriminant of the quadratic equation, it can be shown that a solution exists provided

$$\alpha^2 \geqslant 2\mathrm{Ma}\Delta T_s(0). \tag{40}$$

Thus, for a hump solution to exist when $\mathrm{Bi} = 0$, there is a lower bound on α given approximately by Eq. (40).

When $\mathrm{Bi} \neq 0$, Eq. (39) is replaced with an inequality,

$$\tfrac{1}{2}(3\mathrm{Ma}\Delta T_s(0) - \alpha^2) \geqslant \tfrac{1}{2}(3\mathrm{Ma}\Delta\vartheta(0) - \alpha^2) = -\tfrac{16}{3}\eta^2 + \tfrac{4}{3}\eta\alpha + \tfrac{1}{6}\alpha^2. \tag{41}$$

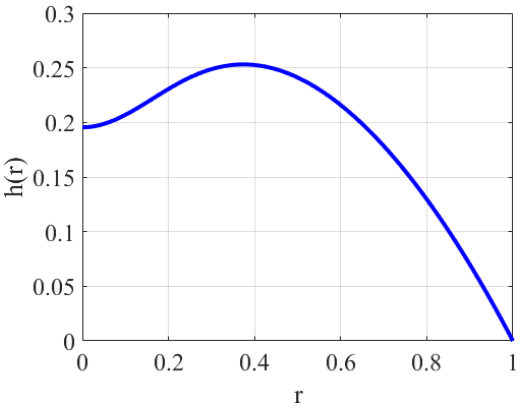

FIG. 7. A specimen hump solution of Eq. (32). Parameters: Ma = 1, $\alpha = 0.2$, $s = 0.2$. Other parameters: Bi = 0 and $\Theta = 0$.

Hence, Eq. (40) still applies as an approximation to the necessary condition for the existence of a hump solution. However, in this case, the hump solution can be expected for a wider range of values than those predicted by Eq. (40). The wider range can be established by looking at the intersection of the graphs of $y_1(\eta) = -(16/3)\eta^2 + (4/3)\eta\alpha + (1/6)\alpha^2$ and

$$y_2(\eta) = \frac{1}{2}(3\mathrm{Ma}\Delta\vartheta(0) - \alpha^2) = \frac{1}{2}\left[\frac{\Delta T_s(0) - \mathrm{Bi}\eta[\Theta + T_s(1)]}{1 + \mathrm{Bi}\eta} - \alpha^2\right]. \tag{42}$$

C. Linear stability analysis

We investigate here the linear stability of the base state $h_0(r)$ with respect to small-amplitude perturbations in the azimuthal direction. For this purpose, we consider a solution $h(r, \varphi, t)$ to Eq. (30) made up of the base state plus a perturbation:

$$h(r, \varphi, t) = h_0(r) + \delta h(r, \varphi)\mathrm{e}^{\sigma t}. \tag{43}$$

As we are concerned here with linear stability with respect to perturbations in the azimuthal direction, we assume that $\delta h(r, \varphi)$ depends in a nontrivial way on φ. We look at the stability of the base state with respect to radial perturbations [hence, $h(r, t) = h_0 + \delta h(r)\mathrm{e}^{\sigma t}$] in Sec. IV, below. We again work with the pinned contact-line boundary conditions, given by Eq. (31c). This enables us to set $\phi = 0$ in Eq. (30), as the interaction forces between the liquid and the substrate are now accounted for in the boundary conditions. We substitute the trial solution $h(r, \varphi, t)$ into Eq. (31c). We assume the perturbations $\delta h(r, \varphi)\mathrm{e}^{\sigma t}$ are small, such that Eq. (31c) can be linearized. The linearized equation for δh is then given by

$$\sigma\delta h + \nabla\cdot\left\{-\tfrac{1}{2}\mathrm{Ma}[2h_0\delta h\nabla\vartheta_0 + h_0^2\nabla(G\delta h)] + \tfrac{1}{3}h_0^3\nabla\nabla^2\delta h + h_0^2\delta h\nabla\nabla^2 h_0\right\} = 0, \tag{44a}$$

where $\vartheta_0(r) = \vartheta(r; h = h_0)$ and

$$G(r) = -\frac{\mathrm{Bi}(\vartheta_0 + \Theta)}{1 + \mathrm{Bi}h_0}. \tag{44b}$$

The boundary condition (31c) becomes

$$\delta h(1, \varphi) = \partial_r\delta h(1, \varphi) = 0. \tag{44c}$$

This is an eigenvalue problem where the eigenvalue σ represents the growth rate: Given a base state, if any of the eigenvalues has a positive real part $\mathrm{Re}(\sigma) > 0$, then the corresponding eigenmode δh grows exponentially and the base state is unstable, otherwise, the base state is stable.

We seek separable solutions of the form $\delta h(r,\varphi) = h_1(r)\mathrm{e}^{\mathrm{i}k\varphi}$. For the present purposes, we assume that $\delta h(r,\varphi)$ has a nontrivial dependence on φ, hence, $k = 1, 2, 3, \ldots$. Equation (44a) then becomes a fourth-order linear ODE:

$$\mathcal{L}(h_1) = \sigma h_1, \quad \mathcal{L} = \sum_{i=0}^{4} A_i(r)\frac{\partial^i}{\partial r^i}, \tag{45a}$$

where the coefficients are given by

$$A_4(r) = \frac{1}{3}h_0^3, \tag{45b}$$

$$A_3(r) = \frac{2h_0^3}{3r} + h_0^2 h_0', \tag{45c}$$

$$A_2(r) = -\frac{2k^2+1}{3}\frac{h_0^3}{r^2} + \frac{h_0^2 h_0'}{r} - \frac{\mathrm{Ma}}{2}h_0^2 G, \tag{45d}$$

$$A_1(r) = \frac{2k^2+1}{3}\frac{h_0^3}{r^3} - (k^2+1)\frac{h_0^2 h_0'}{r^2} + h_0^2(\nabla^2 h_0)' - \frac{\mathrm{Ma}}{2}\left(\frac{h_0^2 G}{r} + 2h_0^2 G' + 2h_0 h_0' G + 2h_0\vartheta_0'\right), \tag{45e}$$

$$A_0(r) = \frac{k^4-4k^2}{3}\frac{h_0^3}{r^4} + 2k^2\frac{h_0^2 h_0'}{r^3} + \nabla\cdot\left(h_0^2\nabla\nabla^2 h_0\right) - \frac{\mathrm{Ma}}{2}\left[-k^2\frac{h_0^2 G}{r^2} + \nabla\cdot\left(h_0^2\nabla G + 2h_0\nabla\vartheta_0\right)\right]. \tag{45f}$$

The boundary conditions at $r = 1$ are given by

$$h_1(1) = h_1'(1) = 0 \;\forall\, k, \tag{46a}$$

and the parity theorem in polar coordinates [20] dictates the boundary conditions at the pole

$$h_1(0) = h_1''(0) = 0, \quad \text{if } k = 1, \tag{46b}$$

$$h_1(0) = h_1'(0) = 0, \quad \text{if } k \geqslant 2. \tag{46c}$$

A Chebyshev tau method is used to solve the eigenvalue problem (45), the full details of which are provided in Appendix C. The results of the stability analysis are summarized graphically, for two distinct paths through the parameter space. These different paths are shown using broken-line curves in Fig. 5(a). The results are shown in Figs. 8 and 9:

(1) Figure 8 shows the largest growth rate $\max_n \mathrm{Re}(\sigma_{k,n})$, where $\sigma_{k,n}$ is the (k,n)th eigenvalue, for wave numbers $k = 1, 2, 3, 4$ as a function of the Marangoni number. The figure corresponds to a constant-contact-angle path in parameter space along which an increase in the Marangoni number has a stabilizing effect.

(2) In Fig. 9, a constant-volume path in parameter space is taken, along which an increase in the Marangoni number is destabilizing.

The abrupt termination of the curves in Fig. 9(a) is due to the loss of the classical solution at a critical Marangoni number, for fixed α. In Figs. 9(b) and 9(c) it is due to the fact that, by following a curve of constant volume in Fig. 5 along a path of decreasing α, the curve eventually terminates at $\alpha = 0$, at a fixed value of Ma. Summarizing, for both paths through the parameter space, $\max_n \mathrm{Re}(\sigma_{k,n})$ remains negative for all considered parameter values. Hence, the classical base-state solution (where it exists) is stable with respect to small-amplitude perturbations in the azimuthal direction.

IV. TRANSIENT SIMULATIONS AND RING RUPTURE

To understand the results of the previous section in more detail, we carry out transient numerical simulations. To allow for droplet spreading and a moving contact line, we use a precursor-film

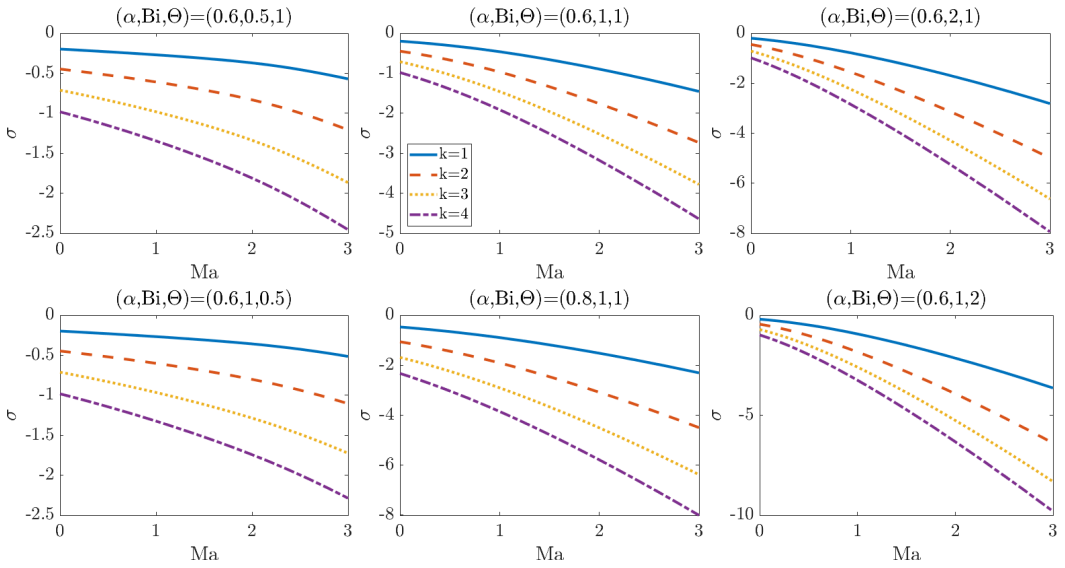

FIG. 8. Dispersion curves for different values of Bi, Θ, and α. Increasing Bi, Θ going across the rows, and increasing α going down the middle column. The value $s = 0.2$ is used throughout.

model [11] extending beyond the droplet core. For this purpose, we use a two-term potential:

$$\phi(x, y, t; h) = \mathcal{A}\left[\left(\frac{\varepsilon}{h}\right)^m - \left(\frac{\varepsilon}{h}\right)^n\right], \tag{47}$$

with $0 < m < n$. Here, ε is the precursor-film thickness. The parameter $\mathcal{A}$ is related to the equilibrium contact angle via the formula [21]

$$\frac{1}{2}\alpha^2 = \frac{\varepsilon\mathcal{A}(n-m)}{(n-1)(m-1)}. \tag{48}$$

The quantities in Eq. (48) are nondimensional, and α is the scaled contact angle. The connection between the scaled contact angle and the unscaled one is given in Appendix A. The contact-line region has a scale of ε. Therefore, to resolve the contact-line region, the simulation resolution should be of the same scale as the precursor-film thickness.

We solve Eq. (30) with the disjoining pressure (47) using a finite-difference scheme on a rectangular grid with equal grid spacing in both directions. The simulation is performed on the domain $(x, y) \in [-L_x, L_x] \times [-L_y, 0]$ with mirror-symmetry boundary conditions. The second-order

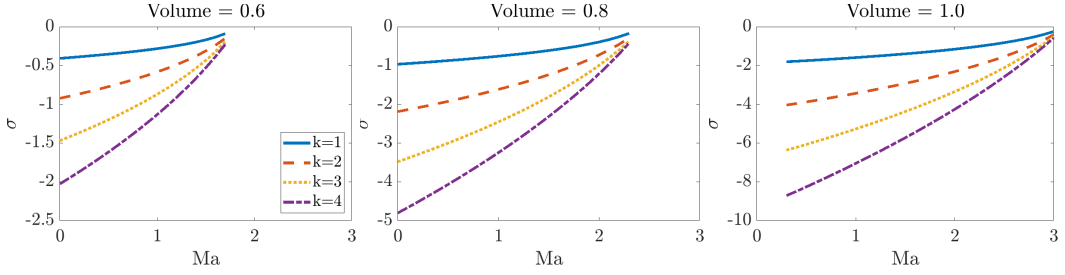

FIG. 9. Dispersion curves for fixed equilibrium droplet volume, where α is allowed to vary. Other parameters are (Bi, Θ) = (1, 1). The value $s = 0.2$ is used throughout.

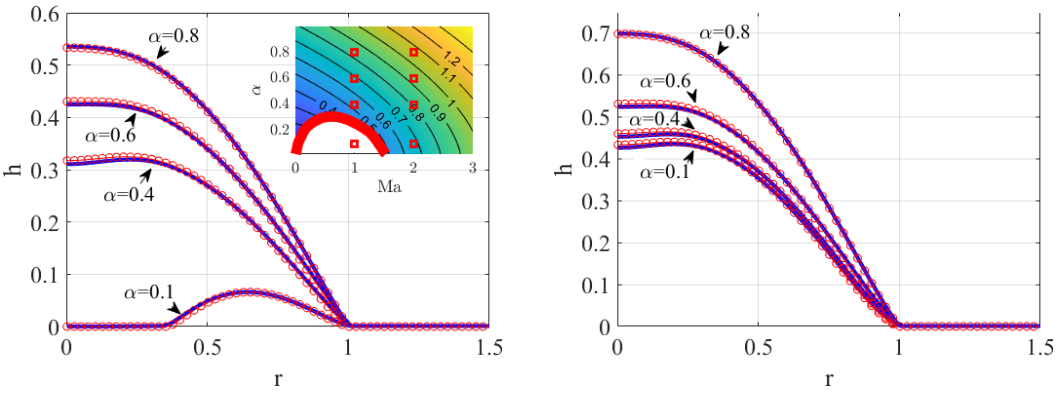

(a) Ma = 1 (b) Ma = 2

FIG. 10. Time evolution of initial states. Lines with circles: the equilibrium solution generated using the boundary-value solvers in Sec. III. Solid lines: the equilibrium solution evolved over 100 dimensionless time units using the precursor-film method. The inset in panel (a) shows the distribution of the parameter values used in the parameter study. We also use a dimensionless precursor-film thickness $\varepsilon = 0.001$. Other numerical parameters are $\Delta x = \Delta y = 0.005$, $\Delta t = 0.05$, and $s = 0.2$.

centered-difference scheme is used to discretize the space domain, and the Crank–Nicolson method is used to discretize the time domain. The discretization produces a system of nonlinear equations for each time step which is solved using a Newton's method [22,23]. A grid-refinement study has been carried out in the context of off-centered heating, which we describe below in Sec. V.

We first of all use the transient simulation technique to address the linear stability of the axisymmetric base-state (32) with respect to axisymmetric perturbations. For clarity, we separate out the different types of linear stability of interest here:

(1) The linear stability analysis of the axisymmetric base state with respect to perturbations in the azimuthal direction [Sec. III, and $k \neq 0$ in Eq. (45) therein].

(2) The linear stability analysis of the axisymmetric base state with respect to axisymmetric perturbations (present section).

The second case can be obtained from setting $k = 0$ in Sec. III, Eq. (45), and by applying the appropriate boundary condition analogous to Eq. (46). However, the numerical eigenvalue solver used in Sec. III proved intractable in this special case, and the dependence of $\max_n(\sigma_{k=0}, n)$ on Ma exhibited some discontinuous features. We therefore study this special case using a different method here. Hence, we pick out a range of parameter values from the Ma-α parameter space and use the axisymmetric solution (32) generated via the shooting method as an *input* into the transient solver. Further initialization is required as part of this process: namely, the introduction of a small precursor film into the axisymmetric solution generated via the shooting method, and the interpolation of same on to a uniform computational grid. This initialization serves as a small-amplitude perturbation. In each case considered, the axisymmetric solution persists after time-marching through 100 time units. Hence, the axisymmetric droplet profile is stable to all perturbations—both axisymmetric and azimuthal. Sample numerical results are shown in Fig. 10. Results are shown for the case $s = 0.2$ but the same results apply for $s = 0.3$. Very little change is observed between initial and final states, confirming the stability of the equilibrium solutions with respect to small axisymmetric perturbations. What little change that is seen is found to reduce even further and to become negligible when the transient numerical solutions are performed with an even smaller value of the precursor-film thickness ($\varepsilon = 10^{-4}$, not shown).

To further illustrate the onset of ring rupture in the low-Ma, low-α part of the parameter space, we solve Eq. (30) to equilibrium with a different initial profile, so that the simulation is started with a droplet-like initial profile with $h(0) \gg \epsilon$. We evolve the system with a homogeneous temperature

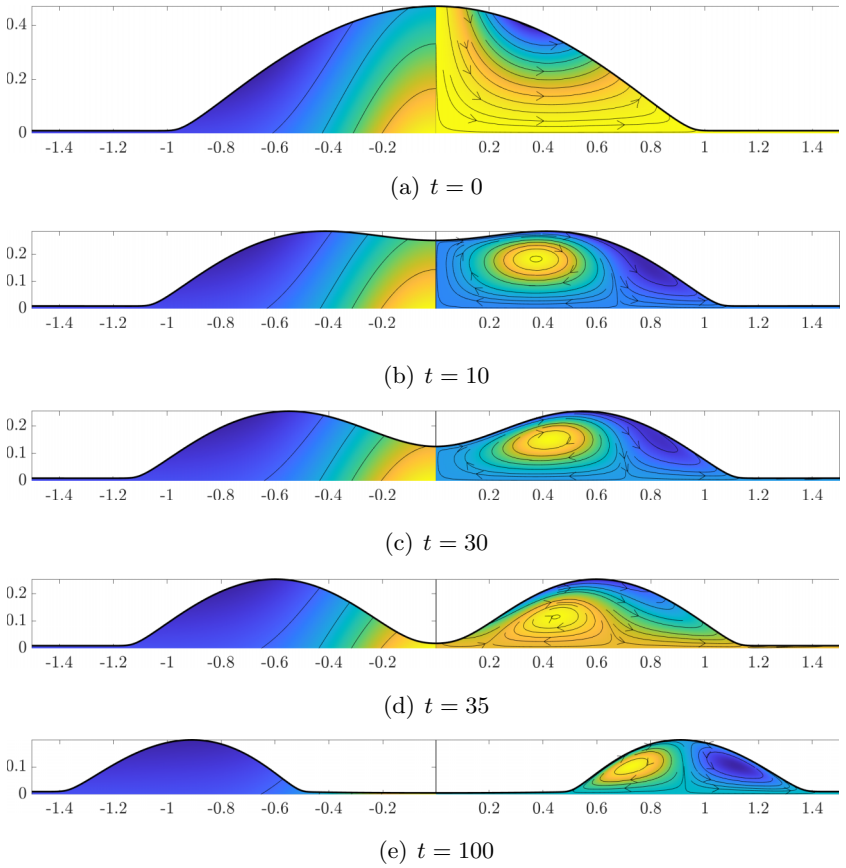

FIG. 11. Evolution of the ring rupture process with axisymmetric heating profile $T_s(r) = \mathrm{e}^{-r^2/0.4^2}$. Relative temperature is shown on the left and the stream function is shown on the right. The scale is maintained throughout the snapshots. The precursor-film parameters are $(\mathcal{A}, \varepsilon, m, n) = (50, 0.01, 2, 3)$ and all other parameters (Ma, Bi, Θ) are taken to be unity. At $t = 0$, the localized heating is turned on and the droplet is no longer at equilibrium, hence the streamlines intersecting with the droplet surface.

profile (i.e., $T_s = 0$) for 100 nondimensional time units until $t = 0$ before turning on the localized heating. The initial condition is axisymmetric with the form

$$h(r, t = -100) = \begin{cases} A(1 - r^2)^2 + \varepsilon, & r \leqslant 1 \\ \varepsilon, & \text{otherwise.} \end{cases} \tag{49}$$

To produce a figure with a suitable aspect ratio that enables a ready interpretation of results, we work with $\alpha = 0.6$. By Eq. (48), this can be achieved with $(\mathcal{A}, \varepsilon, m, n) = (50, 0.01, 2, 3)$. However, in Fig. 5, with $s = 0.3$, this would place us in the no-rupture (droplet) region of the parameter space. Therefore, we use instead $s = 0.4$; it can be checked using the shooting method or `BVP4C` that this parameter combination corresponds to the region of parameter space with rupture.

The evolution towards rupture is shown in Fig. 11. The internal temperature and stream function are plotted. Figure 12 shows the height of the droplet at $r = 0$ throughout the rupturing process. The ring rupture is reminiscent of thin-film rupture driven by thermo-capillary instability [14], which is seen in uniform thin films subjected to heating from below: such films break under the destabilizing influence of the Marangoni force and form more stable droplets [24].

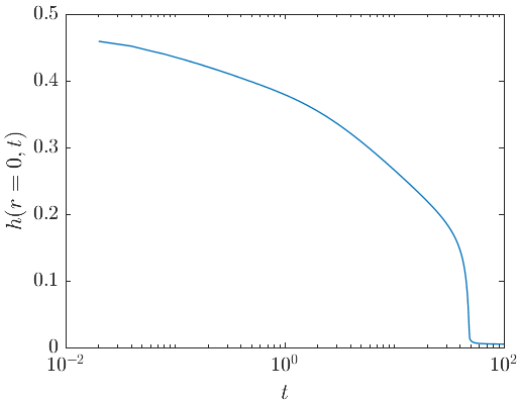

FIG. 12. The height of the droplet at $r = 0$ for the ring rupture process in Fig. 11.

V. OFF-CENTERED HEATING

In this section we consider a temperature hotspot whose center is slightly offset from that of the droplet. As such, we solve Eq. (30) with

$$T_s(x - x_0, y) = \mathrm{e}^{-(x^2+y^2)/s^2}, \tag{50}$$

where $x_0 \ll 1$ is the perturbation, measuring the amount by which the hotspot is off-center. In this scenario, and motivated by Refs. [9,10], we explore mechanisms for producing the kind of flow sketched in Fig. 1. For this purpose, we study the vorticity of the flow inside the droplet. To compute this, we first of all introduce the velocity field in the xy plane:

$$(u, v)(x, y, z, t; h) = -\mathrm{Ma} z \nabla\vartheta + \left(\tfrac{1}{2}z^2 - hz\right)\nabla(-\nabla^2 h + \phi). \tag{51}$$

Hence, the z component of the vorticity is given by

$$\omega_z(x, y, z, t; h) = \frac{\partial v}{\partial x} - \frac{\partial u}{\partial y}. \tag{52}$$

A. Transient simulations

We solve Eq. (30) in a transient mode, using the numerical simulation method and the initial conditions introduced already in Sec. III. We use $\Delta x = \Delta y = 0.01$, $\varepsilon = 0.01$, and $\Delta t = 0.01$. A grid-refinement study with smaller values of $\Delta x = 0.005$ and $\Delta y = 0.005$ indicates that the presented results are robust to changes in the grid resolution. Figure 13 shows a plot of ω_z at the mid-height of the droplet [$z = \max(h)/2$] at $t = 100$ when for $x_0 = -0.01$. Two vortices in the z direction develop within the droplet. The hotspot size s is varied between the two panels. The larger hotspot size in Fig. 13(b). produces a vortex pair of lesser strength but also, more spatially extended.

To understand this effect further, we have plotted the vorticity strength over time in Fig. 14(a). The vorticity strength is taken to be the maximum value of ω_z at a fixed height $z = \max(h)/2$. The figure shows the maximum vorticity first increasing as the externally prescribed asymmetric droplet heating takes effect. This occurs on an $O(1)$ scale in the dimensionless time variable. Thereafter, the vorticity strength rises to a maximum before decaying again to zero. The decay of the vorticity strength corresponds to a "thermotaxis" event where the droplet moves so that its center coincides with the hotspot center, and resumes an axisymmetric equilibrium shape. Thus, the nonaxisymmetry and the associated vortex pair are only a transient event. Evidence of such is shown in Fig. 14(b), where we plot the time evolution of the droplet center. Here, to compute the droplet center, we have computed the x values such that $h(x_1, y = 0, t) = \varepsilon$ and $h(x_2, y = 0, t) = \varepsilon$. For the present purposes, the droplet center is then identified with the midpoint $(x_1 + x_2)/2$.

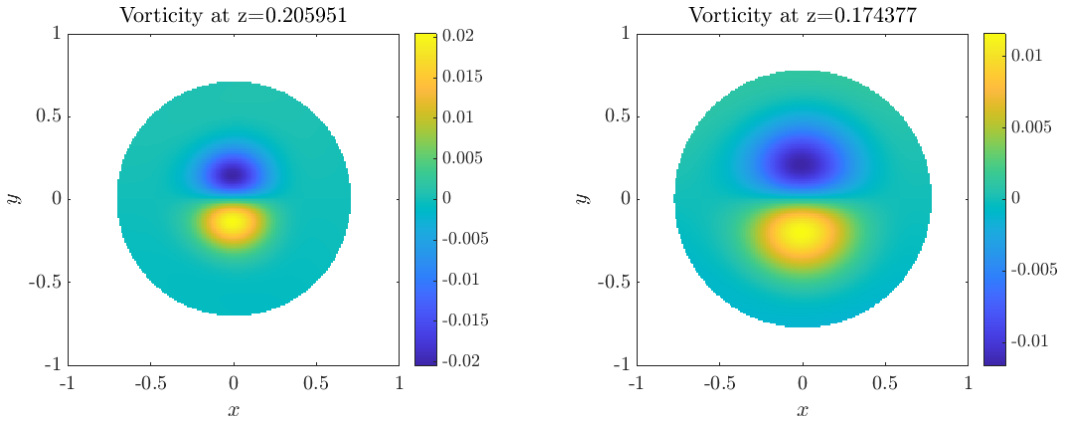

(a) $s = 0.2$ (b) $s = 0.3$

FIG. 13. An xy slice of the z vorticity ω_z in an off-center heated droplet using the precursor film description with different hotspot size. The precursor parameters are $(\mathcal{A}, \varepsilon, m, n) = (50, 0.01, 2, 3)$, heating location at $(x, y) = (-0.01, 0)$, and all other parameters (Ma, Bi, Θ) are taken to be unity.

B. Pinned droplet

The previous transient results reveal that the nonaxisymmetry induced by the off-centered heating is only a transient effect in cases where the droplet contact line can move—in such a case the droplet moves via thermotaxis so as to resume an axisymmetric state. Therefore, to investigate a mechanism for the persistence of nonaxisymmetry, we consider numerical solutions of the basic droplet model (30) with slightly off-centered heating, and with a pinned contact line.

For these purposes, we seek an equilibrium solution as $t \to \infty$ of Eq. (30) for fixed contact line. Hence, we again look at the time-independent equation

$$\nabla \cdot \left\{ -\tfrac{1}{2}\mathrm{Ma} h^2 \nabla \vartheta + \tfrac{1}{3} h^3 \nabla \nabla^2 h \right\} = 0, \tag{53a}$$

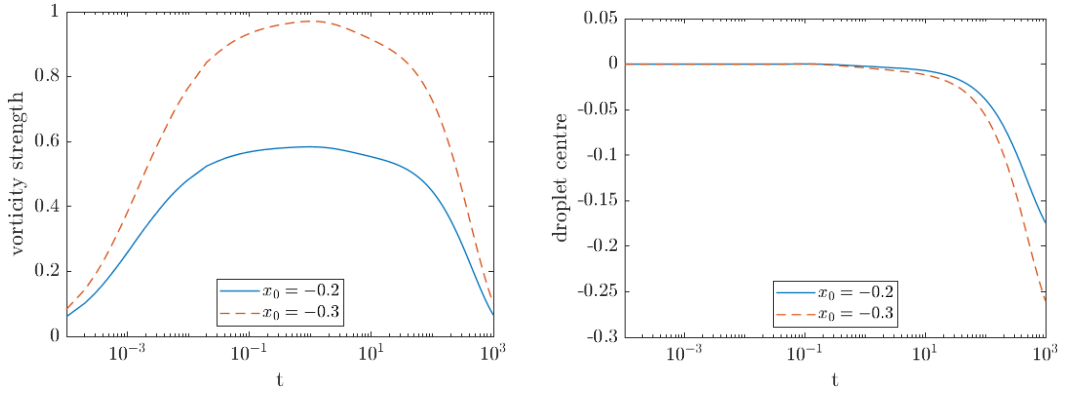

(a) (b)

FIG. 14. Droplet characteristics for two different heating locations: $x_0 = -0.2$ and $x_0 = -0.3$. (a) Time evolution of $\max_{x,y} \omega_z(x, y, z_0, t)$ where $z_0 = \max(h)/2$. (b) Time evolution of the droplet center. Aside from the heating location, all parameters are the same as Fig. 13(a).

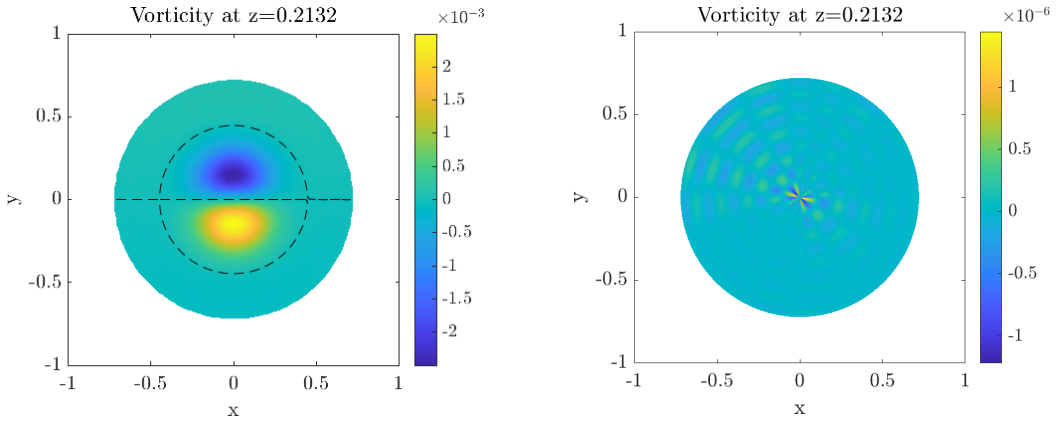

FIG. 15. The z component of the vorticity ω_z with pinned circular contact line at $r = 1$ and $\alpha = 0.6$. (a) Off-centered heating, with hotspot location at $(x, y) = (-0.001, 0)$. (b) Centered heating. Dashed line represents the level-zero contour, which divides the droplet into four circulation regions. All other parameters (Ma, Bi, Θ) are taken to be unity.

with boundary conditions

$$h(1, \varphi) = 0, \quad \partial_r h(1, \varphi) = -\alpha. \tag{53b}$$

For off-centered heating, the solution $h = h(r, \varphi)$ is not axisymmetric. Hence, Eq. (53) must be solved on the disk with $(r, \varphi) \in [0, 1] \times [0, 2\pi)$. A spectral method on the disk is used which gives higher resolution solution compared with the previously introduced finite-difference method. Additionally, using a polar grid removes any spurious fourfold symmetry-breaking which can arise in such simulations due to numerical discretization errors associated with a Cartesian grid. The full details of the numerical method are given in Appendix D. Once the equilibrium solution h is found, the velocity field is computed as

$$u_r(r, \varphi, z; h) = -\mathrm{Ma} z \frac{\partial \vartheta}{\partial r} + \left(hz - \frac{1}{2}z^2\right)\frac{\partial}{\partial r}\nabla^2 h, \tag{54}$$

$$u_\varphi(r, \varphi, z; h) = \frac{1}{r}\left[-\mathrm{Ma} z \frac{\partial \vartheta}{\partial \varphi} + \left(hz - \frac{1}{2}z^2\right)\frac{\partial}{\partial \varphi}\nabla^2 h\right]. \tag{55}$$

The z vorticity is given by

$$\omega_z(r, \varphi, z; h) = \frac{1}{r}\left[\frac{\partial}{\partial r}(r u_\varphi) - \frac{\partial}{\partial \varphi} u_r\right]. \tag{56}$$

Results are shown in Fig. 15. Figure 15(a) shows the vorticity in case of off-centered heating. The vortex pair can be seen clearly. Furthermore, the droplet apex is displaced from $(x, y) = (0, 0)$, although the effect is small. In contrast, in Fig. 15(b) the vorticity in case of centered heating is shown, this is zero, up to numerical error. These results establish two necessary criteria for the existence of persistent loss of symmetry in the flow—off-centered heating and a pinned contact line.

We emphasize finally that temperature at the droplet surface does not exhibit any vorticity signature (e.g., Fig. 16). This makes sense as the temperature equation in the lubrication theory has no advection term, only diffusion. Specifically, the temperature equation is simply $\partial^2 T/\partial z^2 = 0$ [cf. Eq. (9)], with h-dependent surface temperature profile given by Eq. (20). This is consistent with the experimental findings [25], where the authors observed a vorticity signature in the surface

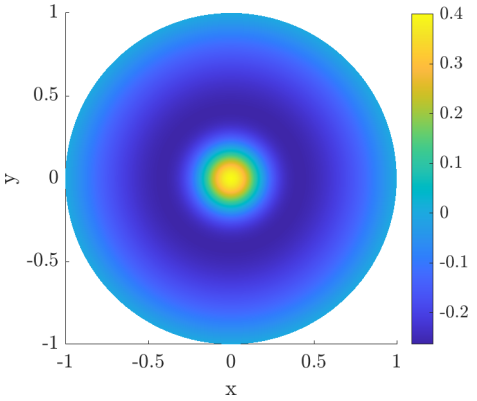

FIG. 16. Relative surface temperature profile $\vartheta(x, y; h)$ of Fig. 15(a).

temperature profile at higher values of contact angle (100°) but not at the lower values of contact angle.

VI. DISCUSSION AND CONCLUSIONS

In this work, we have developed a descriptive model for the generation of azimuthal flows in locally heated droplets. We have drawn inspiration from the experiments in Ref. [10], wherein vortical flows in the azimuthal direction were observed to form spontaneously after the application of localized heating on the substrate. Throughout, we have emphasized the limited applicability of the present analytical model, focused as it is to small equilibrium contact angles. However, an advantage of this approach is the relative simplicity of the mathematical model, which does not require large-scale three-dimensional direct numerical simulation to generate detailed parameter studies. The model also admits some simple mathematical criteria which govern the different kinds of solution types. In spite of these limitations, the model does provide some insights into the vortical flows in locally heated droplets. First, the axisymmetric base state is revealed to be linearly stable with respect to small-amplitude perturbations in the azimuthal direction. Thus, linear stability is ruled out as a mechanism for the generation of vortical flows in the azimuthal direction. A possible explanation for this null result is the lack of feedback of the flow into the temperature equation: in the lubrication scaling, the temperature equation is simply Laplace's equation. Hence, the only nonlinearity in the problem comes from the coupling of the equation for the interface height with the flow field. Feedback of the flow into the temperature equation is likely to become significant when $\epsilon \mathrm{RePr} = O(1)$, where Re is the Reynolds number of the flow inside the droplet and Pr is the Prandtl number [11].

This paper has explored a second mechanism for the generation of nonaxisymmetric flows flows: namely, a small displacement of the center of the heat source from the center of the contact line. Such a displacement gives rise to azimuthal vortical flows, qualitatively similar to those observed in the experiments in Ref. [10]. Our simulations reveal that such vortices die out in the case of depinned droplets: in this case, the droplet moves so as to resume an axisymmetric equilibrium configuration. Our simulations further reveal that the vortices are persistent when the droplet contact line is pinned. Thus, a potential mechanism for the generation and maintenance of such flows has two parts: very slightly off-centered heating combined with contact-line pinning.

Our theoretical results are limited to the hydrophilic case where the equilibrium contact angle is small. Our results in this case are consistent with the experimental findings [25], where the authors observed a vorticity signature in the surface temperature profile at higher values of contact angle (100°) but not at the lower values of contact angle. This work and other works in the series [9,10] used the surface temperature profile to infer the flow structure inside the droplet. The present work,

along with recent DNS results on locally heated droplets [19], suggest that there are flow structures inside such droplets, beyond those which can be inferred by thermal imaging of the droplet surface.

ACKNOWLEDGMENTS

This publication has emanated from research supported in part by a Grant from Science Foundation Ireland under Grant No. 18/CRT/6049. L.O.N. and Y.K. have also been supported by the ThermaSMART network. The ThermaSMART network has received funding from the European Union's Horizon 2020 research and innovation programme under the Marie Sklodowska–Curie grant Agreement No. 778104. We thank an anonymous referee for insights offered and the members of the UCD Fluids Group for helpful comments and suggestions.

APPENDIX A: SCALING OF THE CONTACT ANGLE

In this Appendix we describe the connection between the scaled contact angle and the unscaled one, and we describe how the contact angle is modeled using precursor-film theory.

The relationship between the scaled contact angle and the unscaled one is straightforward and is given by

$$\alpha = \epsilon\widetilde{\alpha},$$

Here, α is the unscaled contact angle and $\widetilde{\alpha}$ is the scaled one. Correspondingly, in unscaled (dimensional) variables, Schwartz [21] describes a relationship between α and the parameters of the potential function in the precursor-film model. The potential function is

$$\phi(x, y, t; h) = \mathcal{A}\left[\left(\frac{\varepsilon}{h}\right)^m - \left(\frac{\varepsilon}{h}\right)^n\right], \tag{A1}$$

and the required functional relationship is

$$\gamma_0(1 - \cos\alpha) = \frac{\varepsilon\mathcal{A}(n - m)}{(n - 1)(m - 1)}. \tag{A2}$$

The scaled parameters (with tildes) of the potential function are

$$\varepsilon = h_0\widetilde{\varepsilon}, \quad \widetilde{\mathcal{A}} = \frac{h_0}{\gamma_0\epsilon^2}\mathcal{A}, \tag{A3}$$

where h_0 is the reference height of the droplet. In the scaled parameters, Eq. (A2) becomes

$$(1 - \cos\epsilon\widetilde{\alpha}) = \epsilon^2\frac{\widetilde{\varepsilon}\widetilde{\mathcal{A}}(n - m)}{(n - 1)(m - 1)}. \tag{A4}$$

When $\epsilon \ll 1$ as in standard lubrication theory, $(1 - \cos\epsilon\widetilde{\alpha})$ is approximated as $\epsilon^2\widetilde{\alpha}^2/2$, and Eq. (A4) becomes

$$\frac{1}{2}\widetilde{\alpha}^2 = \frac{\widetilde{\varepsilon}\widetilde{\mathcal{A}}(n - m)}{(n - 1)(m - 1)}. \tag{A5}$$

This last result is precisely Eq. (48) in the main paper, except that following standard practice, the tildes on the dimensionless variables have been dropped in Eq. (48).

APPENDIX B: DESCRIPTION OF THE SHOOTING METHOD FOR THE BOUNDARY-VALUE PROBLEM

We employ a shooting method to solve the boundary-value problem (31) numerically. The method turns the boundary-value problem into an initial-value problem. As such, we consider the

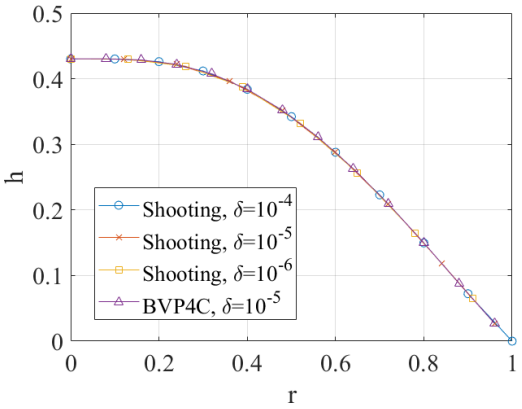

FIG. 17. Plot showing how the shooting method is insensitive to the choice of the regularization parameter δ. Parameter values $\mathrm{Ma} = \Theta = \mathrm{Bi} = 1$, $\alpha = 0.6$, $w = 0.2$.

initial conditions

$$h(0) = p, \quad h'(0) = 0, \quad h''(0) = q. \tag{B1}$$

Given p and q, we use the `ode89` function in MATLAB to solve Eq. (32). The goal now is to find optimal values p and q such that the conditions $h(1) = 0$ and $h'(1) = -\alpha$ are satisfied. To do this, we use the `fminserch` function with a cost function defined by

$$f(p, q) = h(1)^2 + (h'(1) + \alpha)^2. \tag{B2}$$

To ensure that the optimizer terminates at a global minimum and boundary conditions are satisfied, we require f to be less than 10^{-20}. In regions of the parameter space close to where rupture occurs (cf. Fig. 5), the shooting method produces unreliable results, and we revert in those instances to using `BVP4C` in Matlab. In regions of the parameter space far from rupture, the shooting method and `BVP4C` give identical results (e.g., Fig. 17).

Equation (32) becomes ill-conditioned when r or h are small, which occurs at the boundaries. To address this, we approximate the solution with a quadratic function near the boundaries. In practice, instead of solving Eq. (32), we solve

$$h'' = q, \quad r < \delta, \tag{B3}$$

$$h'' = \mathtt{ddh}, \quad |\mathtt{h}| < \delta|\mathtt{dh}|. \tag{B4}$$

Here, `h`, `dh`, `ddh` are the numerical values obtained by the solver at a point just outside the region where the regularization is imposed. We choose a value of $\delta = 10^{-5}$, but our results are insensitive to the values of δ, as shown in Fig. 17.

APPENDIX C: A CHEBYSHEV TAU METHOD FOR THE EIGENVALUE PROBLEM

In this section we describe the numerical Chebyshev tau method used to compute the eigenvalue problem (45) together with the boundary conditions (46). The eigenvalue problem is recalled here in general terms as

$$\mathcal{L}(h_1) = \sigma h_1, \quad \mathcal{L} = \sum_{i=0}^{4} A_i(r) \frac{\partial^i}{\partial r^i}. \tag{C1}$$

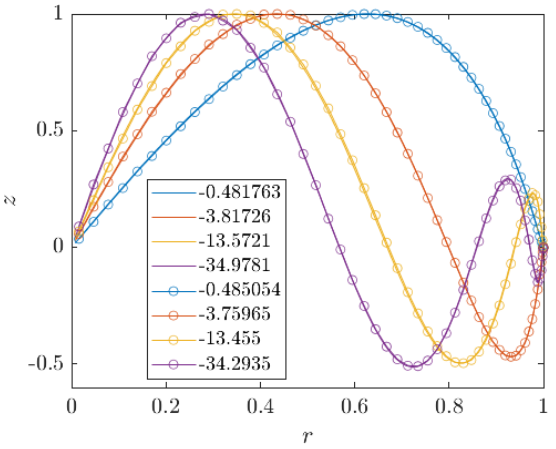

FIG. 18. Plot showing the first four eigenfunctions for $k = 1$. Solid lines: $N = 100$. The legend shows the eigenvalues. Open circles: $N = 50$. Solid lines: $N = 100$. Other parameters: (Ma, Bi, Θ) = (1, 1, 1), $\alpha = 0.6$, and $w = 0.2$.

We start by approximating the solution of Eq. (C1) as a truncated series of Chebyshev polynomials $T_n(x)$ defined on the domain $x \in [-1, 1]$, with coefficients a_n to be determined:

$$h_1(r) = \sum_{n=0}^{N} a_n T_n(2r - 1). \tag{C2}$$

However, it is known that the round-off error can be severe when evaluating higher-order derivatives of the Chebyshev polynomials [26]. To address this, we introduce a new function $g(r) := h_1''(r)$ and rewrite Eq. (C1) as a system of two coupled second-order ODEs:

$$\begin{aligned} &h_1'' - g = 0, \\ &A_4 g'' + A_3 g' + A_2 g + A_1 h_1' + A_0 h_1 = \sigma h_1. \end{aligned} \tag{C3}$$

This avoids the fourth-order derivatives, but we do this at the cost of introducing an additional $N + 1$ unknowns. Hence, we have

$$g(r) = \sum_{n=0}^{N} b_n T_n(2r - 1), \tag{C4}$$

and $2N + 2$ equations are now needed to solve the system. The boundary conditions in Eq. (46) give four equations. Further $2N - 2$ equations are obtained by evaluating Eq. (C3) at the Chebyshev nodes

$$r_i = \cos(i\Delta x), \quad \Delta x = \frac{\pi}{N}, \quad i = 1, \ldots, N - 1. \tag{C5}$$

The generalized eigenvalue problem is then solved using the QZ algorithm with the `eig` function in MATLAB. Sample eigenfunctions showing convergence of the numerical method are provided in Fig. 18.

APPENDIX D: THE SPECTRAL METHOD ON THE DISK

In this section we sketch out the numerical method used to solve Eq. (53a) with the given boundary conditions (53b) (Sec. V), recalled here as

$$\nabla \cdot \left\{ -\tfrac{1}{2}\mathrm{Ma} h^2 \nabla\vartheta + \tfrac{1}{3} h^3 \nabla\nabla^2 h \right\} = 0, \tag{D1a}$$

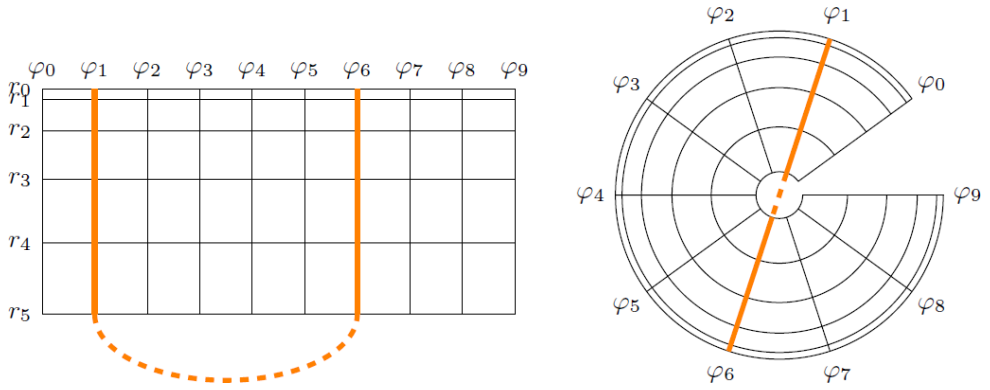

(a) (b)

FIG. 19. Example of (a) a spectral grid in a Cartesian arrangement and (b) the mapping onto a polar arrangement. The pole at $r = 0$ is avoided by construction, the periodic boundary condition is applied in the azimuthal direction, and the only actual boundary is the r_1 row corresponding to the contact line $r = 1$. It is also crucial that every node has a reflection through the origin for the derivatives to be computed.

with boundary conditions

$$h(1, \varphi) = 0, \quad \partial_r h(1, \varphi) = -\alpha. \tag{D1b}$$

Because this problem is no longer axisymmetric due to the off-centered heating, the previously introduced shooting method (Sec. III) is no longer applicable. Instead, we use a spectral method on the disk [27,28]. For these purposes, we use a numerical grid based on equal grids spacings in the φ direction and Chebyshev grid spacing in the r direction. A sketch of the grid is shown in Fig. 19.

The equilibrium solution is found using an iterative method using the expression

$$\nabla \cdot \left[\tfrac{1}{3}(h^n)^3 \nabla \nabla^2\right] h^{n+1} = \nabla \cdot \left[\tfrac{1}{2}\mathrm{Ma}(h^n)^2 \nabla \vartheta^n\right]. \tag{D2}$$

Starting with an initial guess h^0, we solve for h^{n+1} in Eq. (D1a) along with boundary conditions (D1b) in a least-squares sense until the solution converges. The converged solution is then substituted back into Eq. (D1a) to ensure that the residual is small; based on this approach, we use the

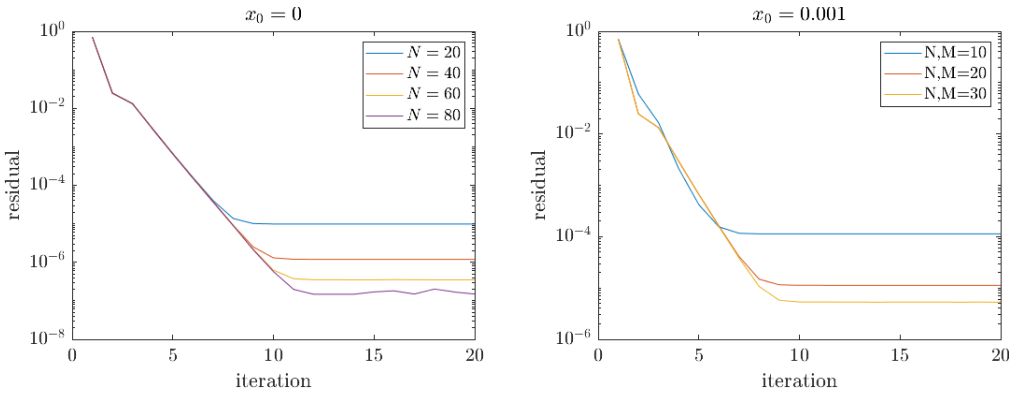

(a) Centered heating (b) Off-centered heating, $x_0 = 0.001$

FIG. 20. Convergence analysis showing the dependence of the residual r_n on N and M. Parameter values: $(\mathrm{Ma}, \mathrm{Bi}, \Theta) = (1, 1, 1)$, $\alpha = 0.6$, and $w = 0.2$. The results have been produced using MATLAB.

residual

$$r_n = \frac{\left\| \nabla \cdot \left[\frac{1}{3} (h^n)^3 \nabla \nabla^2 \right] h^n - \nabla \cdot \left[\frac{1}{2} \mathrm{Ma} (h^n)^2 \nabla \vartheta^n \right] \right\|_2}{\left\| \nabla \cdot \left[\frac{1}{2} \mathrm{Ma} (h^n)^2 \nabla \vartheta^n \right] \right\|_2} \tag{D3}$$

to monitor convergence. We emphasize that this method can only be used to solve for droplets with a circular contact line. A convergence analysis of the method is shown in Fig. 20.

[1] J. Thomson, XLII. On certain curious motions observable at the surfaces of wine and other alcoholic liquors, Philos. Mag. **10**, 330 (1855).

[2] J. Thomson *et al.*, On a changing tesselated structure in certain liquids, Proc. Roy. Philos. Soc. Glasgow **13**, 464 (1882).

[3] P. Ehrhard and S. H. Davis, Non-isothermal spreading of liquid drops on horizontal plates, J. Fluid Mech. **229**, 365 (1991).

[4] H. Bénard, Les tourbillons cellulaires dans une nappe liquide.-Méthodes optiques d'observation et d'enregistrement, J. Phys. Théor. Appl. **10**, 254 (1901).

[5] C. Marangoni, *Sull'Espansione delle Goccie d'un Liquido Galleggianti sulla Superfice di Altro Liquido* (Fratelli Fusi, Pavia, 1865).

[6] H. Fukuyama and Y. Waseda, *High-Temperature Measurements of Materials* (Springer Science & Business Media, Berlin, 2008), Vol. 11.

[7] J. Kim, Spray cooling heat transfer: The state of the art, Int. J. Heat Fluid Flow **28**, 753 (2007).

[8] T. Yano, K. Nishino, S. Matsumoto, I. Ueno, A. Komiya, Y. Kamotani, and N. Imaishi, Report on microgravity experiments of dynamic surface deformation effects on Marangoni instability in high-Prandtl-number liquid bridges, Microgr. Sci. Technol. **30**, 599 (2018).

[9] Y. Kita, A. Askounis, M. Kohno, Y. Takata, J. Kim, and K. Sefiane, Induction of Marangoni convection in pure water drops, Appl. Phys. Lett. **109**, 171602 (2016).

[10] A. Askounis, Y. Kita, M. Kohno, Y. Takata, V. Koutsos, and K. Sefiane, Influence of local heating on Marangoni flows and evaporation kinetics of pure water drops, Langmuir **33**, 5666 (2017).

[11] A. Oron, S. H. Davis, and S. G. Bankoff, Long-scale evolution of thin liquid films, Rev. Mod. Phys. **69**, 931 (1997).

[12] M. J. Tan, S. G. Bankoff, and S. H. Davis, Steady thermocapillary flows of thin liquid layers. i. theory, Phys. Fluids A **2**, 313 (1990).

[13] S. J. Vanhook, M. F. Schatz, J. B. Swift, W. D. McCormick, and H. L. Swinney, Long-wavelength surface-tension-driven Bénard convection: Experiment and theory, J. Fluid Mech. **345**, 45 (1997).

[14] A. Oron, Nonlinear dynamics of three-dimensional long-wave Marangoni instability in thin liquid films, Phys. Fluids **12**, 1633 (2000).

[15] J. B. Bostwick, Spreading and bistability of droplets on differentially heated substrates, J. Fluid Mech. **725**, 566 (2013).

[16] P. J. Sáenz, K. Sefiane, J. Kim, O. K. Matar, and P. Valluri, Evaporation of sessile drops: A three-dimensional approach, J. Fluid Mech. **772**, 705 (2015).

[17] W.-Y. Shi, K.-Y. Tang, J.-N. Ma, Y.-W. Jia, H.-M. Li, and L. Feng, Marangoni convection instability in a sessile droplet with low volatility on heated substrate, Int. J. Therm. Sci. **117**, 274 (2017).

[18] G. Lu, Y.-Y. Duan, X.-D. Wang, and D.-J. Lee, Internal flow in evaporating droplet on heated solid surface, Int. J. Heat Mass Transfer **54**, 4437 (2011).

[19] H. J. Lee, C. K. Choi, and S. H. Lee, Local heating effect on thermal Marangoni flow and heat transfer characteristics of an evaporating droplet, Int. J. Heat Mass Transfer **195**, 123206 (2022).

[20] J. P. Boyd, *Chebyshev and Fourier Spectral Methods*, 2nd ed., Dover Books on Mathematics (Dover Publications, Mineola, 2001).

[21] L. W. Schwartz, Hysteretic effects in droplet motions on heterogeneous substrates: Direct numerical simulation, Langmuir **14**, 3440 (1998).

[22] K. E. Pang and L. Ó Náraigh, A mathematical model and mesh-free numerical method for contact-line motion in lubrication theory, Environ. Fluid Mech. **22**, 301 (2022).

[23] T. Witelski and M. Bowen, Adi schemes for higher-order nonlinear diffusion equations, Appl. Numer. Math. **45**, 331 (2003).

[24] U. Thiele and E. Knobloch, Thin liquid films on a slightly inclined heated plate, Phys. D (Amsterdam, Neth.) **190**, 213 (2004).

[25] A. Askounis, H. Zhang, D. Zhang, Y. Kita, G. Nagayama, M. Kohno, Y. Takata, and K. Sefiane, Unveiling thermocapillary convection in pure water drops, in *International Heat Transfer Conference Digital Library* (Begel House Inc., Danbury, CT, 2018).

[26] J. Dongarra, B. Straughan, and D. Walker, Chebyshev tau-QZ algorithm methods for calculating spectra of hydrodynamic stability problems, Appl. Numer. Math. **22**, 399 (1996).

[27] L. N. Trefethen, *Spectral Methods in MATLAB* (Society for Industrial and Applied Mathematics, USA, 2000).

[28] H. Wilber, A. Townsend, and G. B. Wright, Computing with functions in spherical and polar geometries II. The disk, SIAM J. Sci. Comput. **39**, C238 (2017).